# The Diurnal Cycle of Convection over the Northern South China Sea

**Steven L. AVES and Richard H. JOHNSON**

*Department of Atmospheric Science, Colorado State University, Fort Collins, CO, USA*

(*Manuscript received 7 January 2008, in final form 2 September 2008*)

**Abstract**

The diurnal cycle of convection over the northern South China Sea (SCS) during the onset of the summer monsoon is documented using data from the May–June 1998 South China Sea Monsoon Experiment (SCSMEX) and from ten years of observations from the Tropical Rainfall Measuring Mission (TRMM) precipitation radar.

Results both during SCSMEX and from TRMM observations show a prominent signal of propagating convection over the northern SCS. In particular, convection is found to initiate just off the southern coast of mainland China near sunrise and propagate southeastward at about 10–15 m $s^{-1}$ to the central part of the northern SCS the early afternoon, finally dissipating about 500 km offshore in the late evening. Both indirect measures, such as infrared brightness temperatures and areal cold (< 208 K) convective cloud coverage, and direct measures, i.e., radar reflectivities from the Bureau of Meteorology Research Centre (BMRC) and TRMM radars, show this behavior. The radar data indicate an increasing stratiform contribution to total precipitation as the convective systems move farther offshore, indicative of maturing mesoscale convective systems. Neither advection nor gravity current processes appear to explain the offshore propagation of the envelope of convection, suggesting gravity wave dynamics, possibly associated with discrete propagation, as a factor in the system motion.

## 1. Introduction

Diurnal variation is a prominent feature of the Asian monsoon system. Past studies of the region have noted that the Tibetan Plateau generates significant diurnal variations in vertical motion, diabatic heating, and circulation patterns that exert influence on a continental scale (Nitta 1983; Krishnamurti and Kishtawal 2000; Liu et al. 2007). Others have documented a significant diurnal cycle of proxy variables for convective activity, such as satellite infrared brightness temperatures (e.g., Nitta and Sekine 1994; Ohsawa et al. 2001).

High-resolution studies of convection over Southeast Asia portray a convoluted pattern of the diurnal phase of maximum activity, including the area of the South China Sea (SCS). Typically, over open ocean tropical waters there is an early morning maximum of precipitation (e.g., Gray and Jacobson 1977; Randall et al. 1991; Chen and Houze 1997). However, owing to the complex coastal geometry and topography surrounding the SCS, the diurnal convective behavior deviates from the typical pattern over open oceans. Ohsawa et al. (2001) found an afternoon maximum of convective activity over both land and the interior portion of the SCS region, with early morning maxima most prominent in basins and valleys, along coastlines, and on the windward side of mountains. In most of these areas, mesoscale phenomena such as sea breeze or mountain-valley circulations help to drive the observed diurnal cycle.

The mesoscale processes responsible for the diurnal cycle of convection along coastlines have yet to be fully resolved. During the 1978 Winter MONEX, Houze et al. (1981) examined convective behavior off the northern coast of Borneo using

Corresponding author: Richard H. Johnson, Department of Atmospheric Science, Colorado State University, Fort Collins, CO 80523.
E-mail: johnson@atmos.colostate.edu
©2008, Meteorological Society of Japan

radar and sounding data. The diurnal cycle of the region was dominated by the regular formation of nocturnal mesoscale convective systems (MCSs), which Houze et al. (1981) argued were a result of the low-level convergence of a land breeze and the prevailing monsoon flow. Cells initiated along this convergence line around midnight, organized into convective lines several hundred kilometers long during the morning, and dissipated by early afternoon as they propagated seaward with the prevailing steering-level flow.

Mapes et al. (2003b) found that this land breeze argument was not adequate to describe the diurnal convective behavior offshore over the Panama Bight. Instead, thermally forced gravity waves were proposed as a mechanism for convective initiation across the region. Using a mesoscale model, Mapes et al. (2003b) argued that solar radiation impinging on the raised terrain of the Andes Mountains produced a diurnally oscillating elevated heat source, which generated periodic temperature anomalies around 800 hPa that radiated seaward at around 15 m $s^{-1}$. The warm phase of this anomaly tended to cap convection, while the arrival of the cold phase induced convective development offshore in a manner consistent with observations.

Regardless of the mechanism responsible for convective development and propagation, both Houze et al. (1981) and Mapes et al. (2003b) found that the diurnal phase of maximum convective activity tended to increase with increasing distance from the coast. This is defined as a "propagation signal," or a systematic variation of the phase of maximum convective activity with a coherent spatial structure. Other recent studies have provided observational evidence of propagation signals in the Bay of Bengal (Yang and Slingo 2001; Webster et al. 2002; Zuidema 2003) and off the northern coast of New Guinea (Liberti et al. 2001; Zhou and Wang 2006). In the latter study, Zhou and Wang found that gravity waves generated by deep convective heating over the mountains of New Guinea help to initiate rainbands in the coastal regions offshore.

The 1998 South China Sea Monsoon Experiment (SCSMEX; e.g., Lau et al. 2000) has provided an opportunity for studying convection in the northern SCS, near the southeastern China coast. As will be seen, a southward propagation signal is observed in this region, similar to that found at the Bay of Bengal. An enhanced sounding network, which operated over the region and provided observations every six hours, has already been used to study convective variability and organization during the onset of the monsoon over the SCS (Johnson and Ciesielski 2002; Johnson et al. 2005). Additionally, two Doppler radars in the vicinity of Dongsha Island, approximately 250 km south of the China coast, allowed for direct measures of convective activity. This complements the more indirect satellite proxies which are typically the only available data in other studies of oceanic convection.

This paper focuses primarily on documenting the diurnal behavior of convection over the northern SCS the 1998 SCSMEX year; however, additional data from ten years of TRMM (Tropical Rainfall Measuring Mission) observations are included to substantiate the SCSMEX findings. Several plausible mechanisms are suggested to explain the observed diurnal propagating behavior of convection in this region; however, it is beyond the scope of the study to fully establish the causes of the propagation signal.

## 2. Data and methods

SCSMEX, the major source of data for this study, is an international field experiment aimed at understanding key processes behind the onset and evolution of the summer monsoon over southeastern Asia and the SCS. Figure 1 shows the approximate domain of the SCSMEX experiment, along with locations of sounding stations operating during the study. During the field phase of SCSMEX (1 May–30 June 1998), an extensive network of meteorological and oceanographic instruments was deployed in two sounding/ship arrays, one each in the northern and southern SCS. The array in the northern SCS was centered around the dual-Doppler array composed of radars on Dongsha Island (20.70°N, 116.72°E) and the research vessel R/V *Shiyan* #3 located approximately 20 km southeast of Dongsha Island.

This study utilizes data collected by the Bureau of Meteorological Research Center's C-band polarimetric (C-POL) Doppler radar, which was situated on Dongsha Island during SCSMEX. Table 1 shows a list of the C-POL radar attributes, including physical characteristics, scanning strategy, and types of variables recorded by the radar. The data are interpolated to a Cartesian grid with a horizontal and vertical grid point spacing of 2 and 0.5 km, respectively, and includes volumes of both raw and corrected reflectivities and estimated rainfall rates

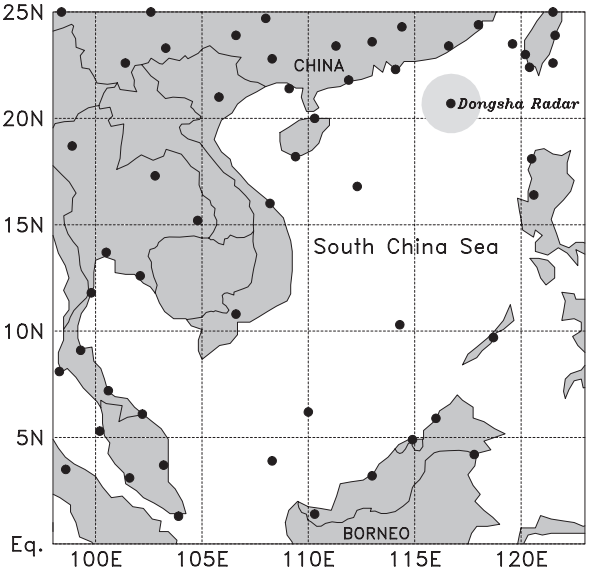


Fig. 1. Overview of the domain and sounding network (dots) surrounding the South China Sea during SCSMEX. Areal coverage of the BMRC C-POL Doppler radar, located on Dongsha Island, is depicted by the shaded circle.

Table 1. Operational characteristics of the BMRC C-POL Doppler radar, which was situated on Dongsha Island during SCSMEX.

| Attribute | Value |
|---|---|
| Radar location | 20°42′11″N 116°43′14″E |
| Altitude | 10 m MSL |
| Peak output power | 250 kW |
| Operating frequency | 5605 MHz |
| Pulse width | 1.0 μs |
| Pulse repetition frequency | 1000 Hz |
| Antenna gain | 45 dB |
| Beam width | 1.0° |
| Maximum range | 300 km |
| Minimum range | 1 km |
| Range resolution | 300 m |
| Scan rate | 10.5° $s^{-1}$ |
| Volume scan frequency | ~600 s |
| Tilt angles (deg.) | 0.5, 1.3, 2, 2.8, 3.9, 4.9, 6.2, 7.5, 9.1, 11.1, 13.5, 16.4, 19.9, 24.1, 29.2 |
| Polarization | Linear Horizontal and Vertical |
| Variables recorded | $Z_H$, $Z_{Hcorrected}$, $V_R$, $\sigma_v$, $Z_{DR}$, $\phi_{DP}$, $\rho_{hv}$ |

based on specific differential phase and differential reflectivity (Bringi et al. 2001).

Since the radar data coverage was limited in both space (to within 250 km of Dongsha Island) and time (reliable data only available in the latter part of May 1998), satellite products are used in this study to supplement radar analyses and extend the results to other periods and locations. The satellite data used are (1) infrared (IR) radiances collected by the fifth generation of the Japanese Geostationary Meteorological Satellite (GMS-5) and (2) precipitation rates based on the TRMM precipitation radar (PR) 2A25v6 algorithm. The GMS data extend over the range of 90°–140°E, 10°S–40°N, and are geometrically corrected to a grid with a constant spacing of 0.05° latitude by 0.05° longitude. The data set has a temporal resolution of 1 h, and extends from 1 May to 30 June 1998 and 2000. The TRMM data are for the May–June post-onset periods for the years 1998–2007. Sounding data are available at 6-h intervals, and are interpolated to a grid with horizontal and vertical spacing of one degree and 25 hPa, respectively. Soundings are quality-controlled and topographic effects are removed using procedures described in Johnson and Ciesielski (2002).

Composite analysis is frequently employed in order to effectively isolate the diurnal cycle. This simple technique averages data from similar times of day to create a composite diurnal time series, from which phase (time of maximum) and amplitude (significance) information can be ascertained. The phase is found by maximizing the linear correlation between the composite time series and a sinusoidal variation with a period of one day. Amplitude is calculated using the discrete formulation of the first Fourier coefficient of the composite time series, and is considered to be the maximum deviation about the mean of the variation, as compared to the maximum high-low difference used in other studies.

Of course, composite analysis assumes the existence of a diurnal cycle. To show that this is a reasonable expectation, Fig. 2 presents a spectral analysis of the areal extent of deep convective cloudiness for May–June 1998, following Hall and Vonder Haar (1999). Deep convective cloudiness is defined as having a black-body IR radiance of < 208 K (Mapes and Houze 1993). The deep convective cloudiness time series is 61 days in length, and is

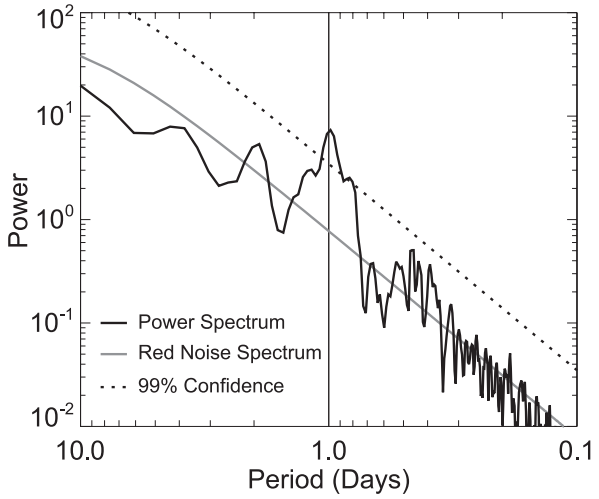


Fig. 2. Power spectrum of the areal cold (< 208 K) cloud coverage time series for the SCS region (10°–25°N, 110°–120°E) during the period 01 May–30 June 1998. Also shown are the accompanying red noise power spectrum and the 99% statistical confidence demarcation.

calculated using the data points located over water in the SCS basin (defined as 10°–25°N, 110°–120°E). To increase the number of independent spectral estimates, the time series was halved, and the resulting power spectra were averaged and smoothed to yield 12 degrees of freedom. Figure 2 clearly shows that the spectral power in the diurnal time range exceeds the 99% confidence interval, validating that a distinct diurnal cycle exists for deep convective cloud cover over the SCS basin.

Other methods are employed to better distinguish convective activity in the IR satellite data. Following Mapes and Houze (1993) and others, the threshold of 208 K is chosen as an indicator of tropical deep convective cloudiness. The Deep Convective Activity (DCA) index of Hendon and Woodberry (1993), given by

$$DCA = \begin{cases} a(230 - T) & T \le 230\,\mathrm{K} \\ 0 & T > 230\,\mathrm{K}, \end{cases}$$

is chosen as the preferred method of estimating precipitation. This index has physical units of mm day$^{-1}$ and is non-zero only for brightness temperatures colder than 230 K. The coefficient a is obtained through a comparison with global satellite-estimated rainfall (Janowiak and Arkin 1991). Finally, the evolution histogram (e.g., Morcrette 1991) is utilized for displaying the relative frequency of cloudiness, such that the diurnal cycle at any brightness temperature (in 4 K bins) can be quickly ascertained.

## 3. Overview of the May–June 1998 summer monsoon onset

The onset of the 1998 monsoon was concurrent with the end of the extreme 1997–98 El Niño event. Regressions of satellite-estimated precipitation against the Niño 3.4 SST index (Ciesielski and Johnson 2006) suggest that El Niño years are characterized by wetter than average conditions over the northern SCS and southern China coast, and drier than average conditions elsewhere in the SCS basin. This was indeed the case in 1998.

Figure 3 depicts the general evolution of the 1998 monsoon through a Hovmöller diagram of IR radiance. The onset of the monsoon, as suggested by the appearance of deep convective clouds over the northern SCS, occurs around 15 May. Ding and Liu (2001) found that this onset was hybrid in nature, caused in part by a midlatitude disturbance as suggested by the southward extension of cold 850 hPa temperature anomalies into the SCS region. Convection commences in the central and southern SCS around 20 May, coincident with the retreat of the western Pacific subtropical high (Liu et al. 2002).

As is often the case, regions of active monsoonal convection (apparent as cool shades in Fig. 3) have several quasi-stationary phases and tend to propagate in a discontinuous fashion (Tao and Ding 1981; Ding and Liu 2001). Frequent convective development occurs over the northern SCS between 15–20 May before shifting into the central and southern SCS, where it remains for around 10 days. An abrupt shift in the cloud pattern is apparent around 1 June when convection commences over the northern SCS and southern China coast for another 10 days. After 11 June, the convective envelope takes another discrete northward step into southern China, where it remained for many days and caused severe flooding in the southern Yangtze River basin (Ding and Liu 2001). Because of the stepwise progression of the convective envelope in Fig. 3, several logical subdivisions are created to better isolate the periods of enhanced convection in the SCS. The MYJN period is defined to extend from 15 May–14 June to encompass the majority of the convective activity apparent in the

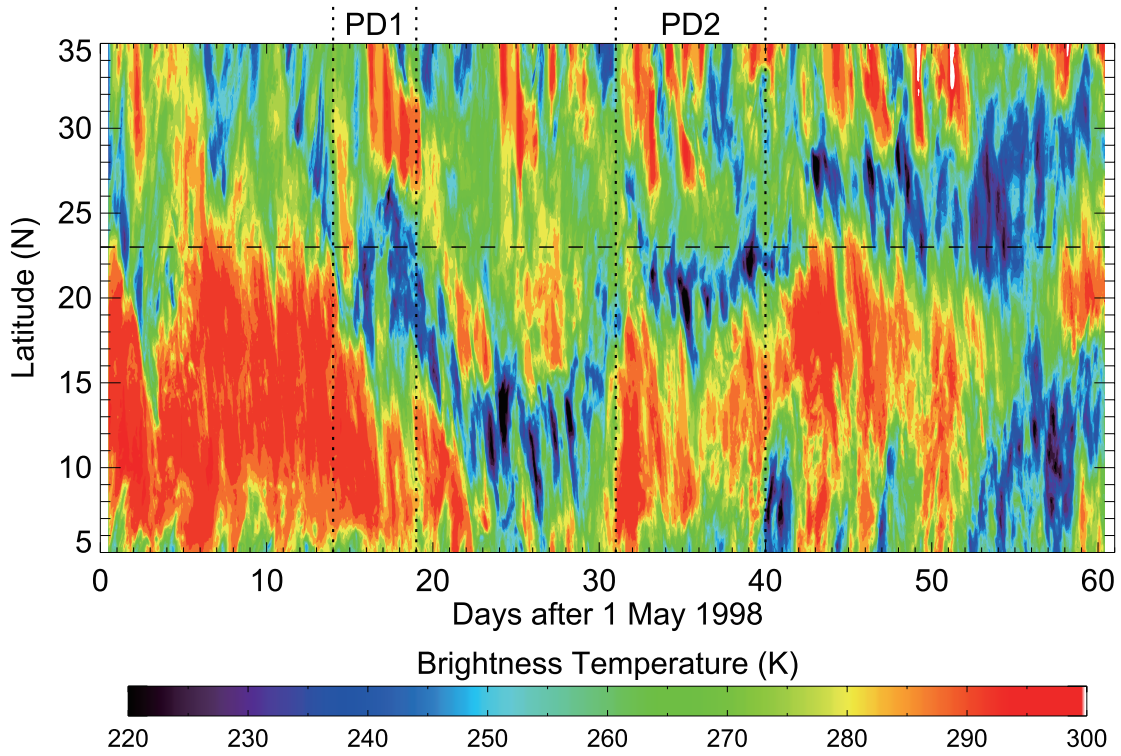


Fig. 3. Latitude-time plot of IR brightness temperatures over the study region. The values along the abscissa are days after 1 May 1998, and cover the range 1 May–30 June. Values shown are brightness temperatures averaged over the 116–117°E longitude band, chosen to coincide with the location of the Dongsha Island radar. The horizontal dashed line at 23°N represents the average location of the southern China coastline within this longitude band. Cool (warm) shades indicate active (suppressed) convective conditions. PD1 and PD2 refer to the first and second convectively active periods, May 15–20 and June 1–10, respectively.

satellite dataset, while periods PD1 (15–20 May) and PD2 (1–10 June) cover the two most active episodes over the northern SCS.

Within regions of active convection, the regular formation and propagation of convective systems is evident are Fig. 3. These systems form on an almost daily basis and preferentially propagate southward, typically over several hundred kilometers before dissipating, and typically take the form of squall lines (Johnson et al. 2005). A similar pattern of activity was found over the Bay of Bengal during the 1999 JASMINE project, as precipitation systems propagated southward from the Indian coast (near 20°N) to the equator (Webster et al. 2002; Zuidema 2003). Radar data from the R/V *Ron Brown* in the Bay of Bengal indicate that these systems had the characteristics of squall lines. The effect that the southward-propagating convective systems in Fig. 3 have on the diurnal cycle of the SCS region is examined in the next section.

## 4. The diurnal cycle of convection over the northern SCS

To further explore the regional diurnal cycle of convection, an analysis of the general diurnal behavior of the entire SCS basin is presented in Fig. 4. The average composite IR brightness temperature time series, calculated for the MYJN period by considering all data points over water within the SCS basin, is at a minimum around 1600 LST. However, the maximum frequency of deep convective cloudiness peaks several hours earlier, around 1200 LST, as shown by the dotted line in Fig. 4. It is important to mention that IR brightness temperatures are not unambiguously related to convection, as any cloud can depress IR radiance from its clear-air value. Even so, IR inferences of convective activity are found to closely match other variables that

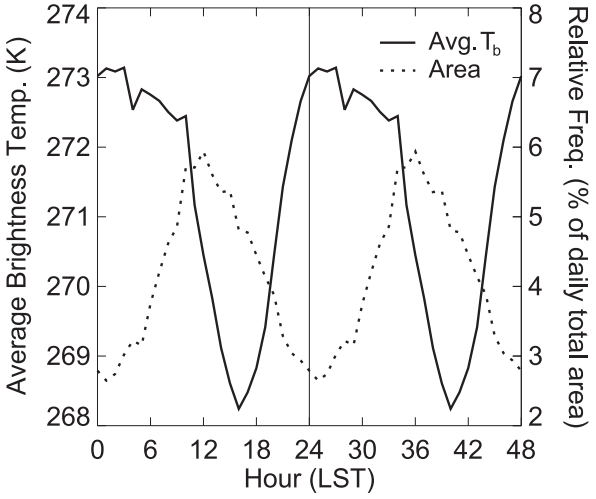


Fig. 4. Basin-wide composite time series of average IR brightness temperature (solid line, left scale) and areal coverage of deep convective cloudiness < 208 K (dotted line, right scale) during the MYJN period (15 May–14 June 1998). All data points over water and within the SCS basin (10°–25°N, 110°–120°E) are included in this analysis.

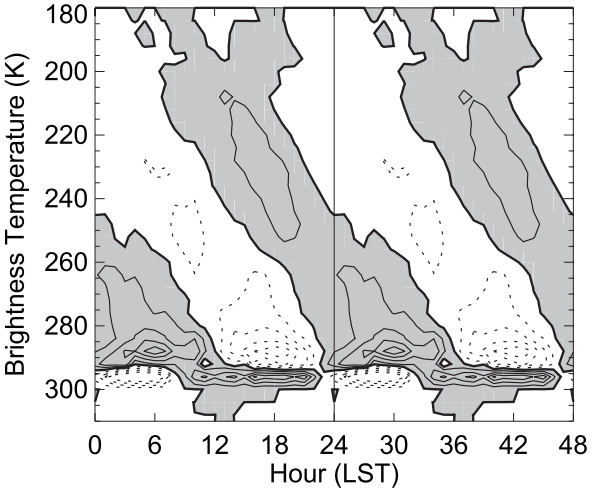


Fig. 5. Basin-wide evolution histogram for the MYJN time period and over the SCS basin. Contours represent percentage anomalies (the contour interval is 0.5), found by subtracting the daily mean histogram of brightness temperature from hourly histograms. Positive anomalies (shaded regions) indicate when cloudiness of a given brightness temperature is more frequent than its average daily occurrence.

are more directly related (such as deep convective cloudiness, DCA, or radar-estimated rainfall) with a 2–4 h lag inherent in IR analyses (e.g., Mapes et al. 2003a). As such, IR analyses will be presented, keeping their limitations in mind, when other data are incomplete or inadequate.

The evolution histogram of IR brightness temperatures (Fig. 5), over the same region during the MYJN period, paints a more complete picture of the diurnal cycle. The coldest cloud tops (around 200 K) occur most frequently around noon LST, with increasingly warmer cloud top temperatures becoming most frequent at successively later times in the afternoon and evening. This gradual increase in cloud-top temperature with time has been related to the decaying cold cloud shields of MCSs in previous studies (e.g., Churchill and Houze 1984). Also in Fig. 5, the diurnal cycle of clear-air return values was inadvertently captured because the average value was close to the delineation between two bins.

While the basin-wide diurnal signal suggests an early afternoon maximum of convection over the SCS basin, additional analysis is required to show how this convective signal evolves spatially. For this purpose, an EOF analysis is used, which determines spatial patterns that best describe the variability in a dataset. Figures 6a–d display the results of an EOF analysis on composite brightness temperatures over the SCS basin, calculated for the MYJN period. Only data points over water were included in the analysis, and a coarser 0.25° square grid was used because of the computational expense of the procedure. The leading and second EOFs are well separated (Fig. 6a), and the associated principle component (PC) time series both have a period of one day (Fig. 6b), effectively capturing the diurnal cycle. Figures 6c and 6d depict the spatial patterns of the leading and second EOF, calculated by regressing the composite brightness temperature time series against the leading and second PC time series, respectively. Values in Figs. 6c and 6d are shaded such that the brightness temperature minimum (and implied convective maximum) in the shaded regions occurs when the associated PC time series is at a maximum.

The leading PC in Fig. 6b suggests a 1600 LST minimum in brightness temperature over the SCS

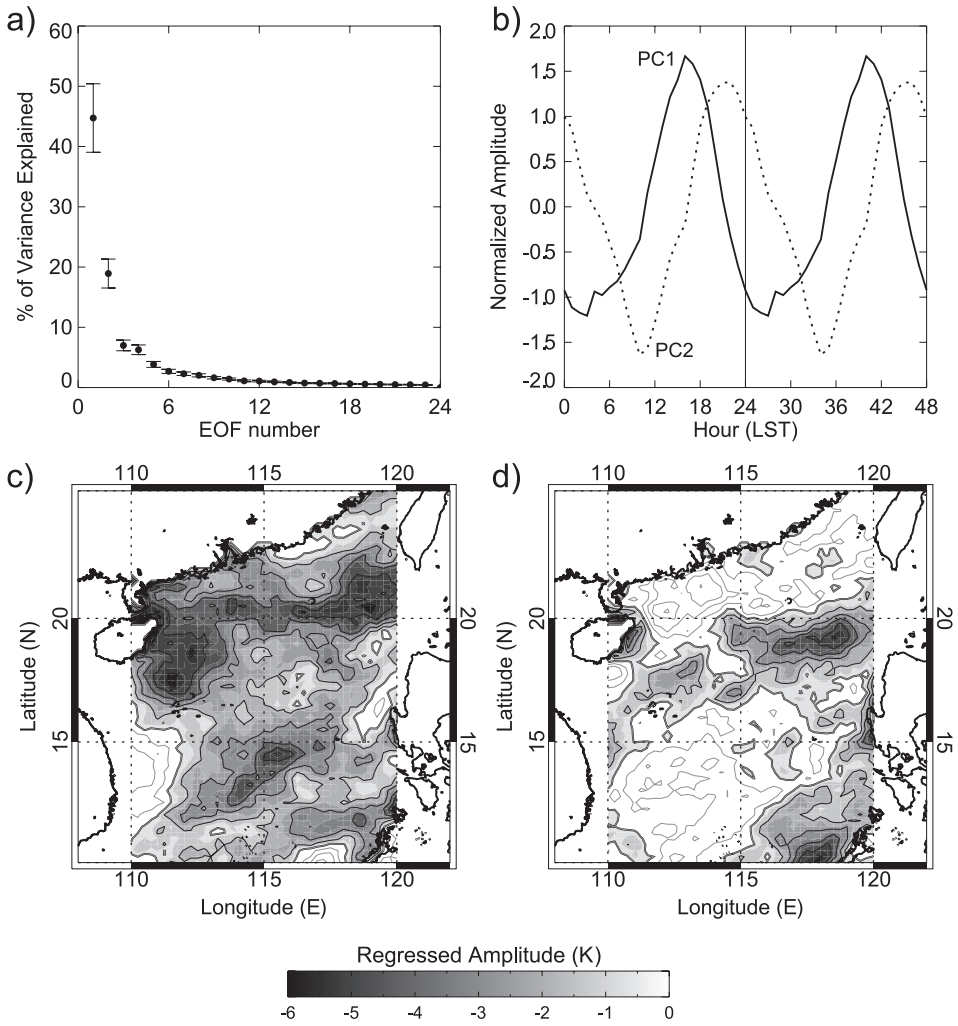


Fig. 6. EOF analysis of diurnal composite brightness temperatures, calculated for the MYJN period over the SCS basin. The variance explained by all EOFs, shown in (a), verifies that the first two EOFs are well-separated. Figure (b) provides the principal component time series for the leading and second EOFs. Figures (c) and (d) show the spatial patterns of the leading and second EOFs, respectively. Contour intervals are 0.5 K in both (c) and (d), and negative values are shaded (negative anomalies of brightness temperature correspond to positive anomalies of convective activity).

basin is consistent with the result in Fig. 4. The leading EOF (Fig. 6c) confirms that this afternoon brightness temperature minimum is a prevalent feature. The maximum regressed amplitudes in Fig. 6c are located in a band a few hundred kilometers south of the China coast. This is partly caused by a local maximum in overall convective activity, and also because the composite time series more closely match PC1 in this area. The second EOF (Fig. 6d) is more complex, suggesting diurnal brightness temperature minima in the morning near the China coast (when PC2 in Fig. 6b is minimized) and in the late evening in the shaded band around 500 km from the coast. The flip-flop nature (morning vs. evening minima) of the phase depiction in Fig. 6d, situated on either side of the highest regressed amplitudes of afternoon minimum in Fig. 6c, provides the impression that a propagation signal may exist over the northern SCS.

The orthogonal requirement of successive EOFs allows further exploration of this propagation signal, as the regressed amplitudes in EOF1 and EOF2 can be used as basis vectors to determine the phase and amplitude of the diurnal cycle (Fig.

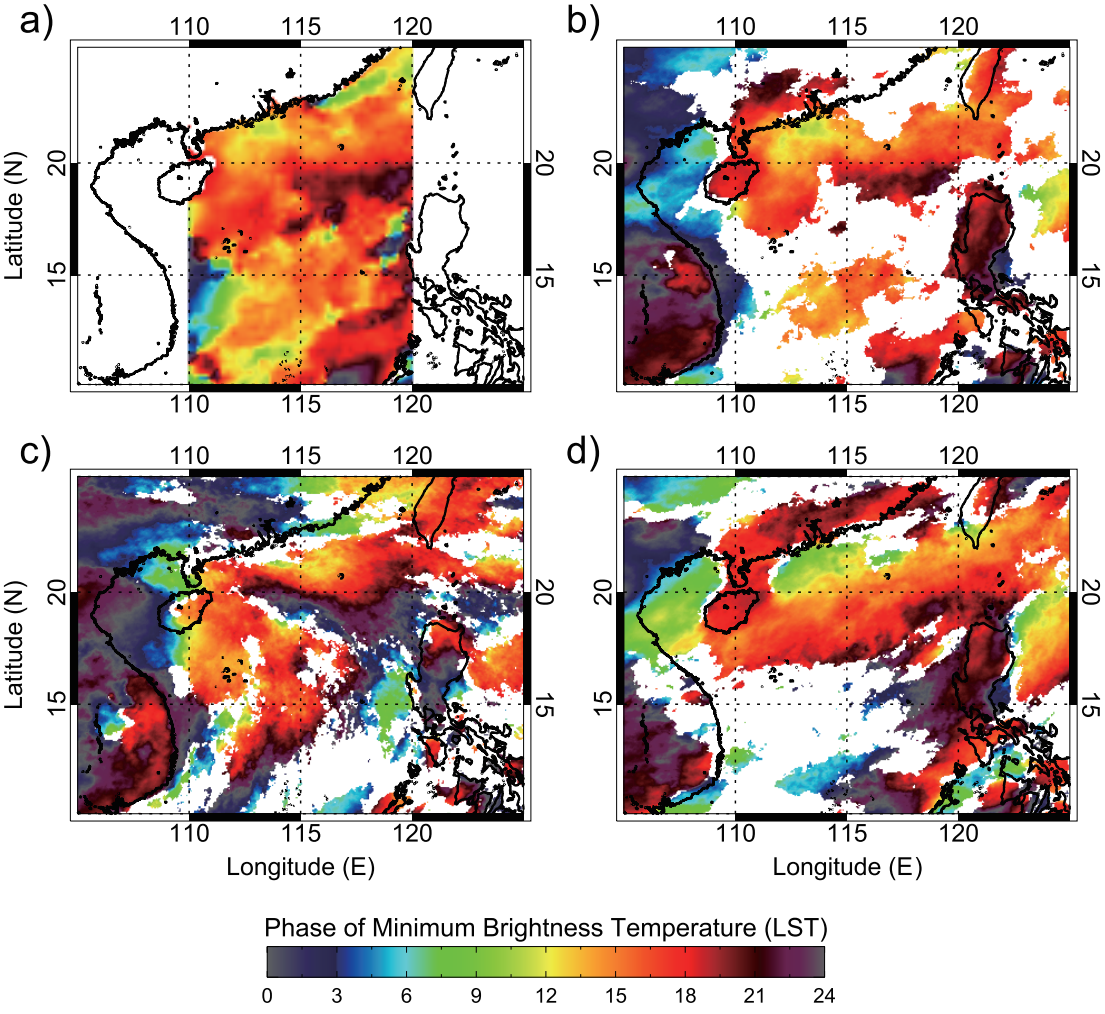


Fig. 7. Spatial distribution of the diurnal phase of minimum IR brightness temperature (and implied maximum convective activity) over the SCS region. Figure (a) was created using the EOF analysis in Fig. 6. Figures (b)–(d) display the phase calculated by fitting a cosine wave to the composite time series of each grid point for the MYJN period in (b), PD1 (15–20 May) in (c), and PD2 (1–10 June) in (d). In (b)–(d), only the data with significant regressed amplitudes (> 3 K) are displayed.

7a). The propagation signal for the MYJN period is clear in Fig. 7a, with a morning brightness temperature minimum just off the southern China coast, gradually increasing to a late evening minimum around 500 km offshore. South of this point the signal becomes more convoluted, as Fig. 7a does not address significance of regressed amplitudes. A simpler and essentially equivalent method of calculating phase and amplitude of the diurnal cycle involves fitting a cosine wave to individual composite time series. Figure 7b is created in this manner for the MYJN time period, and is almost equivalent to Fig. 7a except that insignificant variations (defined as having regressed amplitudes less than 3 K) are not displayed.

Utilizing the cosine-fitting technique described above on composite time series for PD1 (15–20 May) and PD2 (1–10 June), Figs. 7c and 7d compare the two active subperiods to the general MYJN results. In all of panels of Fig. 7, the same propagation signal is apparent to some degree, with morning minima near the coast, progressing to late evening minima as the signal is lost around 300–500 km from shore. Lines of constant phase across the northern SCS are generally parallel to the southeastern China coast, especially in Fig.

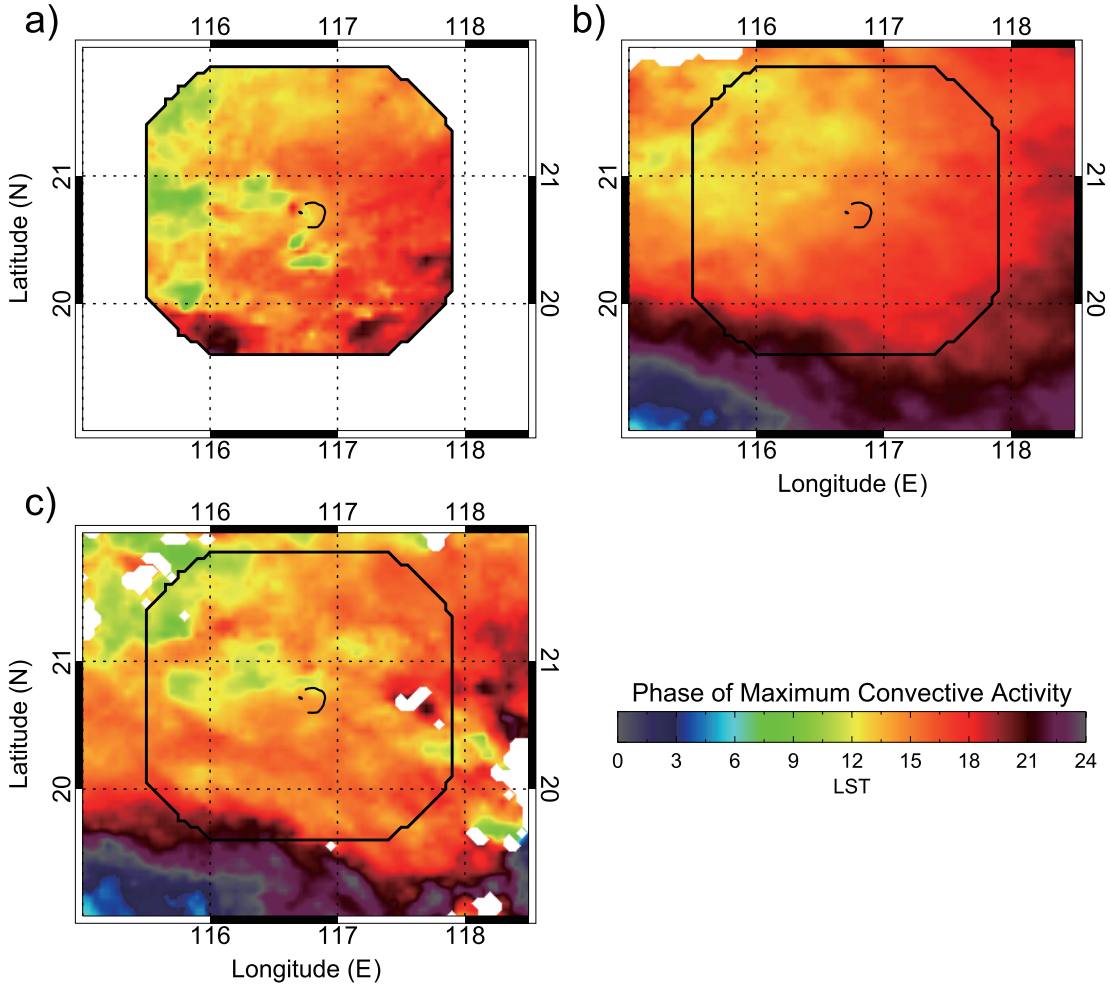


Fig. 8. Phase of maximum convective activity during PD1 (15–20 May), plotted over the BMRC C-POL Doppler radar domain, as suggested by: (a) radar-estimated precipitation, (b) satellite-estimated precipitation (DCA), and (c) infrared brightness temperatures.

7d, consistent with the results of Yang and Slingo (2001) over the Bay of Bengal. A multi-day convective event contributed to the discrepancy along ~ 114°E in Fig. 7c; the phase from north to south along this line is seen cycling through evening, night, and through the next day.

As discussed earlier, propagation signals similar to the one apparent in Fig. 7 have been documented in other regions of the world. However, the operation of the C-POL Doppler radar on Dongsha Island, situated around 250 km south of the China coast, provides a unique opportunity to investigate the propagation signal through more direct measures of convective activity. Figure 8a depicts the diurnal phase of maximum convective activity over the C-POL radar domain for PD1 based on radar-estimated precipitation. For comparison, the phase implied by DCA (Fig. 8b) and IR brightness temperature (Fig. 8c) are displayed for PD1 over the same domain. (For reference, Fig. 9 illustrates the extent of the C-POL Doppler radar coverage over the northern SCS.) Unfortunately the C-POL radar was inoperative during PD2, which was a convectively active period over the northern SCS; thus, radar analyses are restricted to PD1, when convection was most frequent over the radar domain.

The level of agreement among Figs. 8a–c is quite high. All give the same general impression of a propagation signal emanating from the southern China coast, with phase increasing from northwest

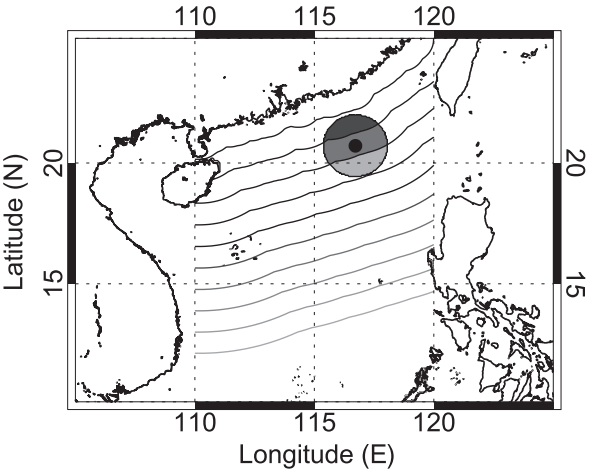


Fig. 9. Isolines of least distance to the southeastern China coast, used to depict convective activity as a function of distance from the China coast. Contour interval is 100 km, and the Dongsha Island radar domain is highlighted.

to southeast across the radar domain. Even more remarkable, the local differences between phases calculated from radar data and DCA are quite small and rarely greater than a few hours. The pattern of phase from IR radiance also qualitatively matches well with radar and DCA interpretations, except that quantitatively they lag by 1–3 hours. The similarity of Figs. 8a–c suggests that satellite data are able to reasonably replicate the diurnal cycle of convection as depicted by the C-POL Doppler radar. This gives confidence to satellite analyses for other periods or locations for which radar data do not exist.

To facilitate the calculation of propagation speeds over the northern SCS, Figs. 10a–b depict the phase of maximum convective activity with respect to distance from the southern China coast in graphical form. To create Figs. 10a and 10b, data points were binned (in 50 km intervals) according to the shortest distance between said point and the coastline, and composite time series were created for each distance bin. As a reference, Fig. 9 illustrates the isolines of shortest distance (in 100 km intervals) over the northern SCS. For satellite analyses, only data points within the longitude range 115°–118°E were included to coincide with the approximate extent of the radar domain.

It is clear in Fig. 10a that for PD1, the propagation signal is represented quite similarly in both satellite and radar data. All suggest a monotonic increase in the phase of maximum convective activity with increasing distance from the coast. Phases calculated using DCA and radar data are within an

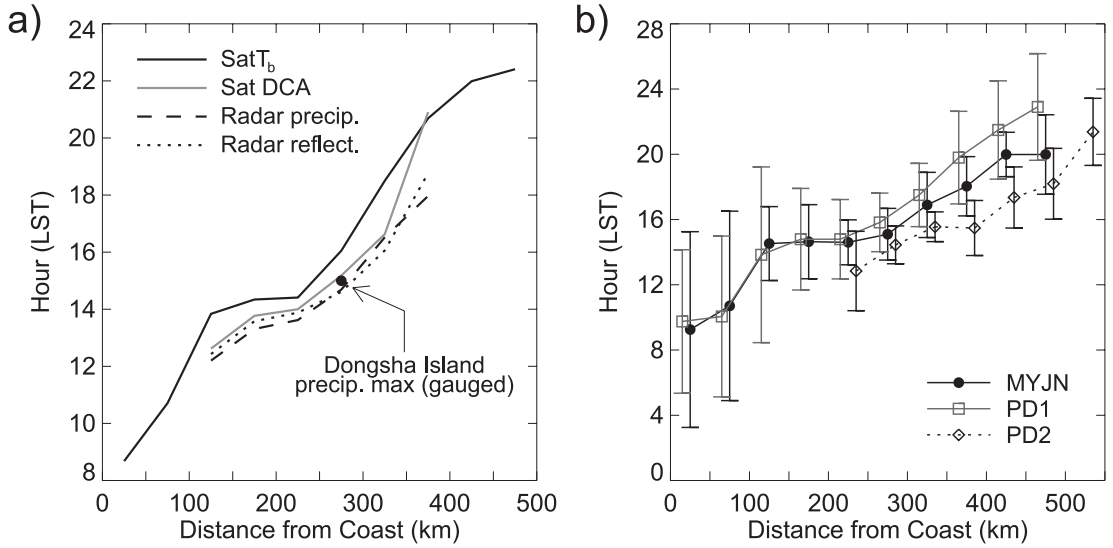


Fig. 10. Phase of maximum convective activity versus distance from the China coast. Figure (a) shows the propagation signal in the convective diurnal cycle among different proxy variables for convective activity (e.g., IR brightness temperature, DCA, radar-estimated precipitation) for PD1 only. In (b), the propagation signal apparent in the IR data is compared for periods PD1, PD2, and MYJN.

hour of each other for most distance bins, while IR phases lag by 1–3 hours. Additionally, the radar and satellite phases for the distance bin of Dongsha Island match with the observed 1500 LST diurnal maximum of rainfall on the island. The level of agreement among independent observation systems suggests that the propagation signal is robust. Regarding propagation speeds, a single value may not be appropriate in Fig. 10a, as the slope changes markedly beyond around 250 km from shore. Best-fit propagation speeds are around 15 m $s^{-1}$ nearer to the coast, and around 10 m $s^{-1}$ beyond this point.

Figure 10b compares the IR brightness temperature propagation signals of PD1, PD2, and MYJN. Error bars (95% confidence) are included by considering the variability of phase within each distance bin, and 3 degrees of freedom are assumed by comparing the longitudinal extent of the distance bin to the average MCS size over the region. Again, a monotonic increase of phase with respect to distance from coast is evident for all periods in Fig. 10b. Error bars for all periods overlap for each distance bin, providing even more confidence that the propagation signal is significant and robust. Propagation speeds are also quite similar, ranging between 10 and 14 m $s^{-1}$.

Another indirect way of showing propagation involves considering the evolution of convective systems as they move southward from the coast of China, because as MCSs mature, their stratiform rain fractions tend to increase (e.g., Houze 1977). To examine this transition over the northern SCS, a convective partitioning algorithm was applied to the C-POL Doppler radar volumes of reflectivity. The algorithm is similar to that of Steiner et al. (1995) with the inclusion of vertical reflectivity data as described in Johnson et al. (2005). The results of this partitioning are presented for PD1 in Fig. 11, binned according to the distance from the China coast. It is clear, with a high degree of consistency ($R^2 \approx 0.8$), that the areal convective fraction decreases with increasing distance from the coastline. This finding is consistent with the idea that MCSs become more mature, i.e., increase their stratiform proportion, as they move farther from the coastline.

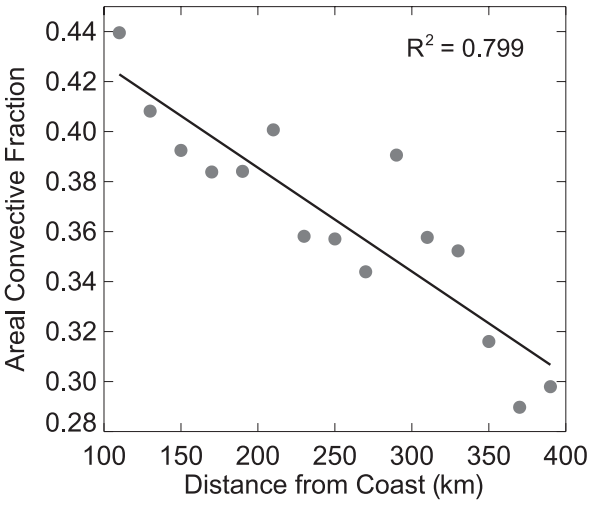


Fig. 11. Areal convective fraction perpendicular to the coast and across the radar domain as a function of distance from the southeast China coast for PD1 (15–20 May).

## 5. Findings for the 2000 La Niña year and ten years of TRMM data

As noted earlier, the 1998 SCSMEX period marked the end of the strong 1997–98 El Niño. To demonstrate the robustness of the results for the single SCSMEX monsoon onset period, two additional data sets and periods have been analyzed: (1) the 2000 May–June monsoon onset period with GMS data, and (2) the 1998–2007 May–June periods with TRMM PR data.

The 2000 onset of the summer monsoon over the SCS region was characterized by much more convective activity over the central and southern SCS than in 1998, and much less activity in the northern SCS and along the southern China coast. This rainfall distribution is consistent with the analysis of Ciesielski and Johnson (2006) for La Niña conditions as occurred in 2000. Although the lack of convection over the northern SCS decreased the regressed amplitudes of composite IR brightness temperature time series, a weak propagation signal was still evident (Fig. 12). Similar to 1998, the implied maximum of convective activity increased with distance from the coast, from 1500 LST around Dongsha Island where the signal first became significant, to the late evening hours around 500 km from shore. The agreement between 1998 and 2000 data in Fig. 12 suggests that the propagation signal may indeed be a regularly occurring feature of the summer monsoon onset, and not just unique to 1998. Observations of a similar propagating signal in the Bay of Bengal (Yang and Slingo 2001; Webster et al. 2002; Zuidema 2003) further

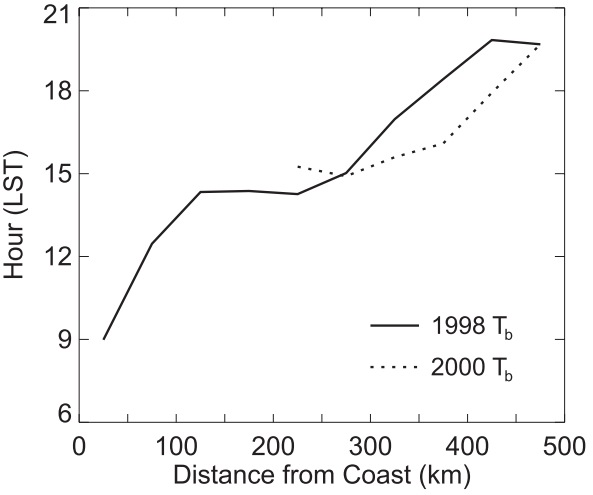


Fig. 12. Phase of the diurnal minimum of brightness temperature versus distance from the southern China coast for similar May-June periods in 1998 and 2000.

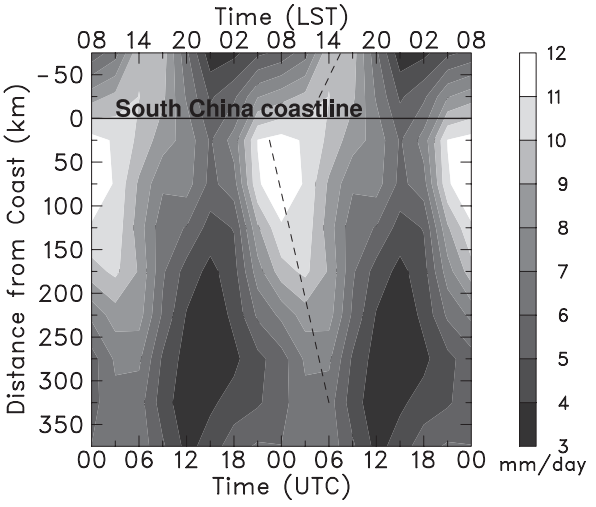


Fig. 13. Hovmöller diagram of diurnal cycle of precipitation as a function of distance from the southern coast of China based on ten years of TRMM 2A25v6 PR data. Two signals of propagation are evident (marked by dashed lines): one offshore starting in the early morning and one onshore during the afternoon.

support the results of this study.

To further substantiate these findings, an additional analysis of ten years of post-onset[1] May–June TRMM PR. These data represent instantaneous values of rain rate with a horizontal footprint of 4.3 km at nadir. Given the narrow swath width (215 km) and coarse sampling in time, the PR data were first averaged into 3-h, 0.25 degree latitude/longitude bins. The use of ten years of data is long enough to sufficiently reduce errors due to sampling issues and provides useful information about the diurnal cycle of convection (e.g., Ichikawa and Yasunari 2006). The PR data were placed into 50-km bins extending seaward from the south China coastline as shown in Fig. 9. Those bins were ~500 km in longitudinal width centered roughly along 115°E. The resulting Hovmöller plot of the diurnal cycle is shown in Fig. 13. Evidence of a propagating signal of precipitation can be seen extending over 300 km from the coastline, with an inferred propagation speed of ~11 m $s^{-1}$. Precipitation begins just offshore in the early morning hours, and reaches 250–300 km offshore by midday. In addition, there is a signal of precipitation forming just onshore around noon and moving inland during the afternoon at ~5 m $s^{-1}$. This precipitation pattern, evident on several days during SCSMEX (Fig. 3), is presumably associated with daytime heating over land and subsequent landward movement of convection in the southwest monsoon flow that frequently occurs after onset (Johnson and Ciesielski 2002).

## 6. Possible propagation mechanisms

This paper has documented a signal of southward propagation of convection over the northern South China Sea during the onset of the summer monsoon. This pattern of propagation continued even when the overall envelope of convection shifted to the central South China Sea. This propagation signal is strikingly similar to that found over the Bay of Bengal during the summer monsoon by Yang and Slingo (2001), Webster et al. (2002), and Zuidema (2003). It is beyond the scope of this paper to fully explain the propagation mechanism(s); however, several possible explanations will be mentioned.

While the low-level flow following monsoon onset is southwesterly, the upper-level winds are typically northwesterly in association with the strong Tibetan anticyclone aloft. The possibility of advection explaining the southward translation of the cloud systems is investigated in Fig. 14, which

1 The onset dates were determined using the NCEP reanalysis 850 hPa zonal wind based on the method outlined in Wang et al. (2004).

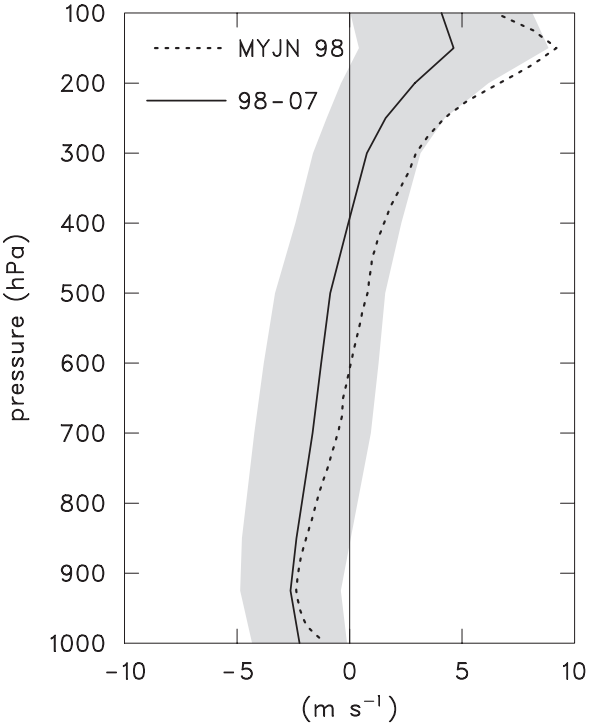


Fig. 14. Vertical profile of the 0800 and 1400 LST average wind component perpendicular to the southern China coast during the 1998 SCSMEX MYJN and the 1998–2007 TRMM periods. Positive wind speeds indicate offshore motion (from NNW to SSE), and the shaded region indicates the standard deviations for the ten-year TRMM period.

shows the vertical profile of the average wind component perpendicular to the southern China coast over the box 18–24°N, 110–120°E during the MYJN 1998 period using the interpolated, gridded SCMEX sounding data and for the 10-year (1998–2007) post-onset mean using NCEP (National Centers for Environmental Prediction) reanalysis data. Figure 14 depicts the average flow for 0800 and 1400 LST, the time period of the propagating convective signal, including standard deviations for the ten-year mean. The typical summer monsoon profile is evident: low-level onshore flow underlying offshore upper-level flow. However, the maximum offshore-directed wind speeds in Fig. 14, about 8 m s$^{-1}$ at the 150 hPa level for 1998 and 5 m s$^{-1}$ for the 10-year mean, are too weak to explain the 10–15 m s$^{-1}$ propagation speeds of deep convection calculated in Section 4. Thus, advection does not appear to be the causal factor in system movement across the region. This flow configuration is similar to that over the Bay of Bengal, where southward-moving convective systems were observed almost paradoxically in an environment of strong southwesterly flow (Yang and Slingo 2001; Webster et al. 2002; Zuidema 2003).

Another possibility involves gravity current dynamics, where systems move according to the strength of the density variation of their cold pools (e.g., Simpson 1987). The speed of a gravity current can be approximated by

$$V = k\left(gH\frac{\Delta\theta_v}{\theta_v}\right)^{1/2} + u_0,$$

where $k$ and the cold pool depth $H$ are assumed to be approximately 1 and 500 m, respectively. The cold pool strength is measured as a perturbation of virtual potential temperature. Cold pools in the vicinity of Dongsha Island were found to be relatively weak, with a virtual temperature perturbation at most of 3 K (Johnson et al. 2005), corresponding to a gravity current speed of 7 m s$^{-1}$ in the absence of a low-level prevailing flow. This speed is too low to account for the observed 10–15 m s$^{-1}$ overall speed of these systems, especially considering that onshore low level flow (Fig. 14) would only serve to lower the estimate of gravity current speed.

Other remaining candidates for system propagation involve gravity wave dynamics. Gravity waves, as described by Mapes et al. (2003b), are capable of communicating information quickly enough to account for the observed propagation speeds over the northern SCS. In Mapes et al. (2003b), it is hypothesized that gravity waves, generated by convergence of turbulent heat flux in the mixed layer during the daytime over the high terrain of the Andes (up to 4 km elevation), propagate westward at about 15 m s$^{-1}$, destabilizing the lower troposphere off the coast of Columbia, South America, after midnight and causing a nocturnal maximum of precipitation over the ocean. The application of this mechanism to the northern South China is problematic since the mountains along the coastline in southern China are relatively shallow, mostly less than 500 m in elevation, and a deep mixed layer to provide this thermal forcing does not exist.

Another candidate mechanism involving gravity waves is contained in the theory of mesohigh/wake low couplets proposed by Haertel and Johnson (2000). Using a linear dynamical model,

Haertel and Johnson (2000) found that evaporative cooling within the broad area of lower-tropospheric cooling in the trailing stratiform regions of squall lines can generate gravity waves that produce mesohigh/wake low couplets at the surface. The gravity wave speed associated with the typical evaporative cooling depth (below the melting level) of 4-5 km is ~12–15 m $s^{-1}$. Squall lines with trailing stratiform regions were observed during SCSMEX (Johnson et al. 2005; their Figs. 8 and 14), so evidence that convective systems to produce such low-level cooling exists. Moreover, the apparent heat source Q1 profiles during the convectively active phases of SCSMEX (Johnson and Ciesielski 2002; their Fig. 13) indicate low-level cooling. However, this mechanism can only be operative after stratiform precipitation regions develop, which means that some other factor must explain the propagation early in the systems' life cycles.

Discrete propagation is yet another way to achieve the observed propagation speeds over the region, as has been observed elsewhere in the tropics (e.g., Houze 1977). Using radar data, line elements within the convective systems were often found to propagate at speeds less than 10 m $s^{-1}$ (Johnson et al. 2005), more in line with the speeds predicted by gravity current theory. Hints of discrete propagation are evident in SCSMEX radar data, with new cells forming to the south of existing lines; however, detailed analysis of this process is beyond the scope of this paper. Shige and Satomura (2001) investigated the mechanism of discrete propagation during TOGA COARE (Tropical Ocean Global Atmosphere Coupled Ocean-Atmosphere Response Experiment) and found that strong upper-level easterlies provided a critical level and ducting of waves that contributed to westward development of eastward-moving convective bands. Fovell et al. (2006) found that discrete propagation can occur when gravity waves generated by a squall line are ducted forward by the storm's own upper-tropospheric leading anvil outflow. Soundings from R/V *Shiyan 3* near Dongsha Island shown in Johnson et al. (2005; their Figs. 9 and 10) indicate that in some instances there was a component of the upper-level offshore flow exceeding 20 m $s^{-1}$, so the existence of a critical level and wave ducting (Shige and Satomura 2001) cannot be ruled out. More work is needed to determine the extent to which this mechanism is operative over the northern SCS.

## 7. Conclusions

The diurnal cycle of convection over the northern South China Sea (SCS) has been investigated using the BMRC C-POL Doppler radar on Dongsha Island in conjunction with GMS-5 IR radiance data for the period 15 May–14 June 1998 during the South China Sea Monsoon Experiment (SCSMEX) and TRMM PR data. The main results of this study are as follows:

- Averaged over the entire SCS basin (10°–25° N, 110°–120°E), the maximum in convective activity occurred during the early afternoon hours. This was true for various satellite proxies of convective activity, including composite brightness temperature time series, deep convective cloudiness frequencies, and evolution histograms. An EOF analysis of brightness temperatures showed that the afternoon maximum was prevalent over most of the SCS basin, in agreement with previous studies of convective activity over the region (e.g., Nitta and Sekine 1994; Ohsawa et al. 2001).
- The diurnal cycle of convection over the northern SCS can only be fully explained within the context of diurnally propagating convection from the southeastern China coastline. A propagation signal was quite evident over the northern SCS, with the diurnal phase of convective maximum increasing with distance from the coast, from the early morning hours along the coast, to the late evening hours where the signal was lost around 500 km from the coast. A similar result was found for the period 1998–2007 using TRMM PR data, but the signal weakened approximately 300 km offshore.
- Whereas other studies have shown a similar propagation signal in satellite data (e.g., Yang and Slingo 2001; Liberti et al. 2001; Mapes et al. 2003b), the propagation signal over the northern SCS was shown to exist similarly in both satellite and radar data, with both phase and propagation speed in agreement. Propagation was also implied by the increase in the stratiform fraction of convective systems moving southward away from the coast, suggesting maturing MCSs as they move southward.[2]

2 TRMM PR data for the period 1998-2007 also indicate increasing stratiform rain fraction offshore, from 47% in the coastal region to 52% 350 km from the coast.

- The propagation signal was deemed to be robust, as it appeared similarly using independent observation systems, including ten years of TRMM PR data. Comparisons of results from two active subperiods with the main period of study were also quite similar, adding to the confidence in the results. Finally, a weak but similar propagation signal was found in 2000, which was a convectively unfavorable year in the northern SCS.
- The relatively fast propagation speeds (10–15 m $s^{-1}$) of the envelope of convection could not be adequately explained using advective or gravity current mechanisms. Gravity wave dynamics, possibly associated with discrete propagation, may therefore explain the relatively fast motion of these convective systems.

Considering that similar propagating signals of convection linked to the diurnal cycle are found in other parts of the world, further work is needed to understand the mechanisms for propagation. Further work with SCSMEX radar data is needed to investigate the nature of the convective systems and the extent to which discrete propagation is occurring. The propagation characteristics over the SCS are similar to those over the Bay of Bengal – southeastward motion in an environment of low-level southwesterly flow (Yang and Slingo 2001; Webster et al. 2002: Zuidema 2003) – so it is possible that similar mechanisms are operative in these two important monsoon oceanic regions.

## Acknowledgments

This research has been supported by the National Aeronautics and Space Administration under Grants NNG04GA22G and NNX07AD35G. The helpful comments of two anonymous reviewers are appreciated. We thank Paul Ciesielski for his considerable help throughout this project, Tom Keenan and Michael Whimpey for their assistance with the BMRC C-POL radar data, Kathy Straub for supplying monsoon onset dates, and Rick Taft for his careful editing of the manuscript.

## References

Bringi, V.N., T.D. Keenan, and V. Chandrasekar, 2001: Correcting C-band radar reflectivity and differential reflectivity data for rain attenuation: a self-consistent method with constraints. *IEEE Trans. Geosci. Remote Sens.*, **39**, 1906–1915.

Chen, S.S. and R.A Houze, Jr., 1997: Diurnal variation and life-cycle of deep convective systems over the western Pacific warm pool. *Quart. J. Roy. Meteor. Soc.*, **123**, 357–388.

Churchill, D.D. and R.A. Houze, Jr., 1984: Development and structure of winter monsoon cloud clusters on 10 December 1978. *J. Atmos. Sci.*, **41**, 933–960.

Ciesielski, P.E. and R.H. Johnson, 2006: Contrasting characteristics of convection over the northern and southern South China Sea during SCSMEX. *Mon. Wea. Rev.*, **134**, 1041–1062.

Ding, Y.-H. and Y. Liu, 2001: Onset and evolution of the summer monsoon over the South China Sea during SCSMEX field experiment in 1998. *J. Meteor. Soc. Japan*, **79**, 255–276.

Fovell, R.G., G.L. Mullendore, and S.-H. Kim, 2006: Discrete propagation in numerically simulated nocturnal squall lines. *Mon. Wea. Rev.*, **134**, 3735–3752.

Gray, W.M. and R.W. Jacobson, Jr., 1977: Diurnal variation of deep cumulus convection. *Mon. Wea. Rev.*, **105**, 1171–1188.

Haertel, P.T. and R.J. Johnson, 2000: The linear dynamics of squall line mesohighs and wake lows. *J. Atmos. Sci.*, **57**, 93–107.

Hall, T.J. and T.H. Vonder Haar, 1999: The diurnal cycle of west Pacific deep convection and its relation to the spatial and temporal variation of tropical MCSs. *J. Atmos. Sci.*, **56**, 3401–3415.

Hendon, H.H. and K. Woodberry, 1993: The diurnal cycle of tropical convection. *J. Geophys. Res.*, **98**, 16623–16637.

Houze, R.A., Jr., 1977: Structure and dynamics of a tropical squall-line system. *Mon. Wea. Rev.*, **105**, 1540–1567.

Houze, R.A., Jr., S.G. Geotis, F.D. Marks, Jr., and A.K. West, 1981: Winter monsoon convection in the vicinity of North Borneo. Part I: Structure and time variation of the clouds and precipitation. *Mon. Wea. Rev.*, **109**, 1595–1614.

Ichikawa, H. and T. Yasunari, 2006: Time-space characteristics of diurnal rainfall over Borneo and surrounding oceans as observed by TRMM-PR. *J. Climate*, **19**, 1238–1260.

Janowiak, J.E. and P.A. Arkin, 1991: Rainfall variations in the tropics during 1986–1989, as estimated from observations of cloud-top temperature. *J. Geophys. Res.*, **96**, 3359–3373.

Johnson, R.H. and P.E. Ciesielski, 2002: Characteristics of the 1998 summer monsoon onset over the northern South China Sea. *J. Meteor. Soc. Japan*, **80**, 561–578.

Johnson, R.H., S.L. Aves, P.E. Ciesielski, and T.D. Keenan, 2005: Organization of oceanic convection during the onset of the 1998 east Asian summer monsoon. *Mon. Wea. Rev.*, **133**, 131–148.

Krishnamurti, T.N. and C.M. Kishtawal, 2000: A pro-

nounced continental-scale diurnal mode of the Asian summer monsoon. *Mon. Wea. Rev.*, **128**, 462–473.

Lau, K.M., Y. Ding, J.-T. Wang, R.H. Johnson, T. Keenan, R. Cifellia, J. Gerlach, O. Thiele, T. Richenbach, S.-C. Tsay, and P.-H. Lin, 2000: A report of the field operations and early results of the South China Sea Monsoon Experiment (SCSMEX). *Bull. Amer. Meteor. Soc.*, **81**, 1261–1270.

Liberti, G.L., F. Chéruy, and M. Desbois, 2001: Land effect on the diurnal cycle of clouds over the TOGA COARE area, as observed from GMS IR data. *Mon. Wea. Rev.*, **129**, 1500–1517.

Liu, X., J. Wang, G.X. Wu, X.Y. Liang, W.P. Li, and Y.M. Liu, 2007: Numerical modeling of the influence of Eurasian orography on the diurnal change of summer atmospheric circulation. *Chinese J. Atmos. Sci.*, **31**, 389–399.

Liu, Y., J.C.L. Chan, J.Y. Mao, and G.X. Wu, 2002: The role of Bay of Bengal convection in the onset of the 1998 South China Sea summer monsoon. *Mon. Wea. Rev.*, **130**, 2731–2744.

Mapes, B.E. and R.A. Houze, Jr., 1993: Cloud clusters and superclusters over the oceanic warm pool. *Mon. Wea. Rev.*, **121**, 1398–1415.

Mapes, B.E., T.T. Warner, M. Xu, and A.J. Negri, 2003a: Diurnal patterns of rainfall in northwestern South America. Part I: Observations and context. *Mon. Wea. Rev.*, **131**, 799–812.

Mapes, B.E., T.T. Warner, and M. Xu, 2003b: Diurnal patterns of rainfall in northwestern South America. Part III: Diurnal gravity waves and nocturnal convection offshore. *Mon. Wea. Rev.*, **131**, 830–844.

Morcrette, J.-J., 1991: Evaluation of model-generated cloudiness: satellite-observed and model-generated diurnal variability of brightness temperature. *Mon. Wea. Rev.*, **119**, 1205–1224.

Nitta, T., 1983: Observational study of heat sources over the eastern Tibetan Plateau during the summer monsoon. *J. Meteor. Soc. Japan*, **61**, 590–605.

Nitta, T., and S. Sekine, 1994: Diurnal variation of convective activity over the tropical western Pacific. *J. Meteor. Soc. Japan*, **72**, 627–641.

Ohsawa, T., H. Udea, T. Hayashi, A. Watanabe, and J. Matsumoto, 2001: Diurnal variations of convective activity and rainfall in tropical Asia. *J. Meteor. Soc. Japan*, **79**, 333–352.

Randall, D.A., Harshvardhan, and D.A. Dazlich, 1991: Diurnal variability of the hydrologic cycle in a general circulation model. *J. Atmos. Sci.*, **48**, 40–62.

Shige, S. and T. Satomura, 2001: Westward generation of eastward-moving tropical convective bands in TOGA COARE. *J. Atmos. Sci.*, **58**, 3724–3740.

Simpson, J.E. 1987: *Gravity Currents in the Environment and the Laboratory*. John Wiley & Sons, New York, 244 pp.

Steiner, M., R.A. Houze, Jr., and S.E. Yuter, 1995: Climatological characterization of three-dimensional storm structure from operational radar and rain gauge data. *J. Appl. Meteor.*, **34**, 1978–2007.

Tao, S.-Y. and Y.-H. Ding, 1981: Observational evidence of the influence of the Qinhai-Xizang (Tibet) plateau on the occurrence of heavy rain and severe convective storms in China. *Bull. Amer. Meteor. Soc.*, **62**, 23–30.

Wang, B., Y. LinHo, and M.-M. Lu, 2004: Definition of South China Sea monsoon onset and commencement of the East Asia summer monsoon. *J. Climate*, **17**, 699–710.

Webster, P.J., E.F. Bradley, C.W. Fairall, J.S. Godfrey, P. Hacker, R.A. Houze, Jr., R. Lukas, Y. Serra, J.M. Hummon, T.D.M. Lawrence, C.A. Russell, M.N. Ryan, K. Sahami, and P. Zuidema, 2002: The JASMINE pilot study. *Bull. Amer. Meteor. Soc.*, **83**, 1603–1630.

Yang, G.-Y. and J. Slingo, 2001: The diurnal cycle in the tropics. *Mon. Wea. Rev.*, **129**, 784–801.

Zhou, L. and Y. Wang, 2006: Tropical Rainfall Measuring Mission observation and regional model study of precipitation diurnal cycle in the New Guinean region. *J. Geophys. Res.*, **111**, D17104, doi:10.1029/2006JD007243.

Zuidema, P., 2003: Convective clouds over the Bay of Bengal. *Mon. Wea. Rev.*, **131**, 780–798.